Arabian Journal for Science and Engineering (2021) 46:2527–2541
https://doi.org/10.1007/s13369-020-05145-7

RESEARCH ARTICLE-MECHANICAL ENGINEERING

Reproducibility of Replicated Trabecular Bone Structures from Ti6Al4V Extralow Interstitials Powder by Selective Laser Melting

Arif Balcı[1] · Furkan Küçükaltun[1] · M. Fatih Aycan[1] · Yusuf Usta[1] · Teyfik Demir[2]

Received: 10 April 2020 / Accepted: 11 November 2020 / Published online: 3 January 2021

Abstract
The field of orthopedic regenerative medical studies has begun to use porous metal structures for biomedical implants, which have lower strength and ingrowth behavior, similar to bones. It is possible to produce such porous metal structures with a designable microarchitecture or replicated topology by additive manufacturing. The main purpose of using these artificial pore geometries in the biomedical field is to increase the biocompatibility of the product by imitating the bone. In this study, bone samples from the femoral and vertebral regions of a sheep were obtained and scanned by microfocus computed tomography (Micro-CT). Trabecular bone models were produced from Ti6Al4V extralow interstitials powder using the selective laser melting with 1:1, 1:1.25, and 1:1.50 scales. The produced samples were scanned using Micro-CT, and 3D models were formed. The 3D models of the trabecular bone and samples were aligned in a computer environment to determine deviations in both size and angle of arms in the trabecular structure. It was found that the deviations decreased when the angle was above 60°, whereas they significantly increased with the size below 150 microns. The size distribution and interconnectivity ratio of the pores formed in the production was obtained from the PNMs. It was determined that the mean equivalent diameters of vertebra and femoral pores, from the pore network models are 767 ± 265 μm and 623 ± 245 μm, and concluded that the samples produced in the scale of 1: 1 and 1: 1.25 could represent the pore size distribution in the bone.

Keywords Trabecular bone · Selective laser melting (SLM) · Additive manufacturing · Porous metals

1 Introduction

A bone has a hierarchical structure that affects its mechanical, biological, and chemical properties because this hierarchical structure consists of compact and trabecular bones in a macro scale. A compact bone has a porosity of 3–5%. Osteocytes, canaliculi, blood vessels, and erosion gaps are present in these cavities. Unlike the compact bone, there are larger pores in the trabecular bone and the proportion of these cavities reaches up to 90%. The gaps in the trabecular bone are connected to each other in a network; thus, the interconnected structure of bone is as important as its trabecular pore size for tissue development and osseointegration [1–5].

In addition to the bone hierarchical structure, the bone has a dynamic mechanism that can renew itself. Osteoclasts play a role in the resorption of bone tissue, whereas osteoblasts provide new bone formation [6]. The unique and self-renewing dynamic mechanism of the bone allows its affected areas to be repaired in case of damage. However, if the damage in the bone structure is too large to repair itself, complementary components must be added to the damaged area [7]. Autograft and allograft are adopted as complementary tissues in the repairment of bone structures. On one hand, the use of allograft is not favorable because it is difficult to obtain and susceptible to disease transmission. On the other hand, autograft causes secondary diseases in surgical regions [8]. Due to these uncertainties, studies aiming to

✉ Teyfik Demir
tdemir@etu.edu.tr

Arif Balcı
arifbalci@gazi.edu.tr

Furkan Küçükaltun
furkankucukaltun@gmail.com

M. Fatih Aycan
mfaycan@gazi.edu.tr

Yusuf Usta
yusta@gazi.edu.tr

[1] Mechanical Engineering Department, Gazi University, Ankara, Turkey

[2] Mechanical Engineering Department, TOBB ETÜ Universty, Ankara, Turkey

develop suitable biomaterials in addition to tissue usage have begun. Biomaterials should have four main characteristics determined by Hutmacher [9]. In these characteristics, biomaterials have to allow natural cell growth and have similar natural mechanical properties on the damaged area. Pores of a biomaterial should have appropriate size and network structure for transporting nutrients and waste. Its surface structure has to be suitable for bone ingrowth and vascularization [9].

Metallic implants with porous lattice structures can simulate the structure of the bone. They also allow bone regeneration and ingrowth as opposed to solid materials [10, 11]. Metallic noncellular biomaterials have higher elastic modulus (e.g., Young's Modulus is approximately 210 GPa for CoCrMo, 110 GPa for Ti6Al4V, and 190 GPa for 316L stainless steel) than bone structures (the Young's Modulus of trabecular bone ranges from 0.02 to 2 GPa, whereas that of the cortical bone ranges from 3 to 30 GPa) [12, 13]. Due to the major difference between metallic biomaterials and bone, a "stress shielding effect" occurs, which causes bone instability, implant loss, and bone resorption [14]. Biomaterials that have characteristics similar to the bone structure with reduced mechanical properties might be a solution to stress shielding effect [15]. In preliminary studies, it has been observed that the advantages of additive manufacturing allow the production of complex porous structures. The controlled production of these structures provides an isentropic or functionally graded porous cage structure, which can be designed according to the properties of the application area to mimic the mechanical and biological properties of bone [16, 17]. Therefore, the lattice structured biomaterials, pore size, and three-dimensional properties should be taken into consideration in order to increase the ratio of interconnectivity to osseointegration. In the studies on the effect of pore size on tissue development, there was no vascularization in the pores smaller than 50 μm [18]. Cartilage tissue was formed in the pores ranging from 90 to 120 μm in size, and the bone grew when the pore size was over 350 μm [19]. A pore size of 300–400 μm was found to be the most suitable for direct Haversian type bone formation (including capillaries and marrow) [20]. Lipid and bone marrow deposition occurs at a gap size of 400–600 μm, which deteriorates the mechanical properties [19, 21, 22].

Porous lattice geometries can be obtained, drawing inspiration from artificial architectures and natural formations, by scanning. Artificially formed lattice architectures are found in metal foams, polymer foams, and porous ceramics, and occur naturally in bone, wood, sponge, and stones [16]. These porous structures have many applications in aerospace, automotive, and medical industries. Lattice structures can be classified as open or closed and can be in a random or symmetrical distribution. Conventional processes (such as freeze casting, gas foaming, and particle leaching) obtained by the production of pore architectures have a random pore distribution. Because of this random distribution, the development of new blood capillary and the transportation of oxygen-nutrient are prevented due to deviations in the course of blood capillaries [23, 24]. In the studies related to the three-dimensional architecture of porosity, the focus was on the structures with open pores and regular arrangement, which can provide the connection of the pores located within the structure. The use of structures with regular support arms has shown that stress can be consistently distributed to all elements in the structure [25, 26]. Promising results have been obtained in the use of symmetrical cubic structures in the production of biomaterials using additive manufacturing [25, 27–29]. In addition to cubic symmetric lattice, studies on the structure of diamond [25, 26, 30, 31], truncated cube [26], truncated cuboctahedron [25, 26], tetrahedron [32], rhombicuboctahedron [26], and octet truss [32] have been carried out to determine the properties for the use of unit cell lattice structures in orthopedic implants [16]. Additionally, irregular pore formation as well as the bone structure and imitation of bone biomimetic studies are included in the literature [33, 34]. In biomimetic studies, Voronoi diagrams and variables have been used to create microlattice structures that can mimic bone structure with different combinations of pore distribution and geometry. In the study of Barack et al., the mechanical properties of different dimensions of the same model were examined for models obtained by micro-CT scanning chimpanzee bone. Due to the fact that the average trabecular bone thickness is higher than 3D printing resolution, it has been observed that dimensional changes are low in the production of the designed geometry [35]. Similarly, the sheep bone trabecular structure model was obtained by Wood et al. and it was examined that the mechanical strengths of the samples rotated at an angle of different degrees in the same region of obtained structure were produced by 3D printing and their mechanical strength [36]. In the study of Cheng et al. [37], the human femur was copied with Micro-CT and 12, 24 and 36 repetitions of sample models with low medium and high porosity ratios were produced from Ti6Al4V Grade 5 powder by selective laser sintering and the strength of the produced disc samples were examined. When the studies on the production of bone structure by copying were examined, it was determined that there were studies on the mechanical strength and biological properties of different geometries produced from polymer material with 3D printing and metal material with SLS. However, the effect of SLM production on the change in trabecular arms and pore size distribution has not been studied [38].

The geometrically complex parts, for which the capabilities of conventional production methods are insufficient, can be produced with SLM which is an additive manufacturing method with powder bed fusion [38, 39]. In SLM method, the melt pool is formed by heating the selected area in the powder bed by laser beam [38]. As the laser beam moves away from

the area, the melt pool rapidly cools and solidifies. With the melting of the relevant section of the part, the building platform goes down to the specified layer thickness and the new powder bed layer is laid from the powder feed unit through the spreader. The process of melting and creating a new powder layer continues until the part geometry is completed. On the other hand, deviations have occurred during the production of porous geometry properties which include a melting mechanism and unsupported production [40]. Because of not using a support structure and powder melting mechanism, sagging, waviness and changes in the centerline of the structural elements have been occurred [40–43]. In the study of Mazur et al. [43], they observed that production capability decreased and deviation increased by decreasing the angle with the table plane for SLM. Moreover, it was concluded that under 100 micron diameter and under 20° positional angle, productions failed.

The SLM has a completely melting mechanism in which undesirable internal closed pores may occur in the final microstructure [44–47]. It has been determined that the pores in the structure could be spherical or sharp cracks. The pores with a sharp crack shape are created by insufficient energy density or agglomeration, while spherical pores are caused by trapped gas and high energy density [48–56]. Sharp crack-shaped pores are a major undesirable defect in terms of crack initiation and damage due to high stress concentration [38]. Important parameters affecting pore formation include laser power, scanning speed, powder layer thickness, hatch distance, powder bed temperature, and focused beam plane distance [38]. In the study of Stef et al. [57], the pore equivalent diameters ranged from 4 to 40 μm, while the average pore size was 11 μm. In another study on pore defect size, Voisin et al. [58] found a pore size up to 60 microns in equivalent diameter.

The aim of this study is to investigate the productibility of a porous metal bone structure which simulates sheep trabecular bone. In this study, the replicated trabecular structures which obtained from the vertebra and femur of a sheep by Micro-CT method were produced from Ti6Al4V ELI alloy powder by the SLM. The trabecular sheep bones and SLM samples pore size distribution were compared by using pore network models. In addition to the examination of trabecular porosity, the geometry and dimensional distribution of closed pores were also examined within the scope of investigation of changes in production.

2 Material and Method

2.1 Micro-CT of Bone and Modeling

The bone samples from which the trabecular structure was replicated were taken from the femur and vertebral regions of a 22-month-old sheep. Bone samples were cut for Micro-CT without large damage and stored in 10% formaldehyde solution. The bone samples were scanned in a wet formaldehyde environment using Bruker Skyscan 1272: 8 micron scanning pixel size, 90 kV source voltage, 111 mA source current, and an Al 0.5 + Cu 0.038 mm filter. The cross-sectional images of the horizontal slice plane to be used to create with the 3D models were created with NRecon software from the obtained scanning data. The 3D computer-aided design (CAD) model was created by identifying the grayscale areas of the bone at Mimics software. Damaged areas formed while cutting the bone for Micro-CT and cortical bone, whereas epiphyseal plaque disrupted the simplicity of the trabecular structure (Fig. 1). By removing these areas, cylindrical models were created.

2.2 SLM Production and Analysis of Samples

The cylindrical models were produced with SLM. In the production, support structures were not used to keep cavities in the porous structure. A circular plate was placed at the bottom of the sample according to the growing direction. Productional geometries were scaled at 1:1, 1:1.25, and 1:1.50 since they were aimed at investigating the reproducibility of different pore sizes of the trabecular structure. A Concept Laser M2 Cusing machine was used for SLM. The working parameters of SLM are given in Table 1. Ti6Al4V ELI Grade 23 (CL41) powder from Concept Laser GmbH was used as a raw material in this production. The powder used complies with ASTM F136-2a standard, and the chemical composition of the powder is given in Table 2.

The produced samples were removed from the table and heat treated in an argon atmosphere. During the heat treatment, the samples were first heated up to 840 °C in 4 h and maintained at this temperature for 2 h. Then, they were cooled to 500 °C in the furnace. After that, they were allowed to cool in air atmosphere from 500 °C to room temperature.

Jeol JSM 6360 LV scanning electron microscope was used in the examination of the produced samples. Its scanning voltage was 26 kV and its spot diameter was 60 μm. The samples were cut parallel to the building plane to reveal the internal cross-sectional view. Additionally, a Leica CTR6000 microscope was used for the optical imaging of the cross-sectional views.

2.2.1 Determination of Deviations in Production Models

In order to examine the deviations in trabecular bone production, the powder remaining in the porous samples after SLM production was evacuated with compressed air and ultrasonic cleaner. In addition, the analysis of the change in porosity ratio in production was made by using 3D models obtained by scanning data from samples. Micro-CT was performed

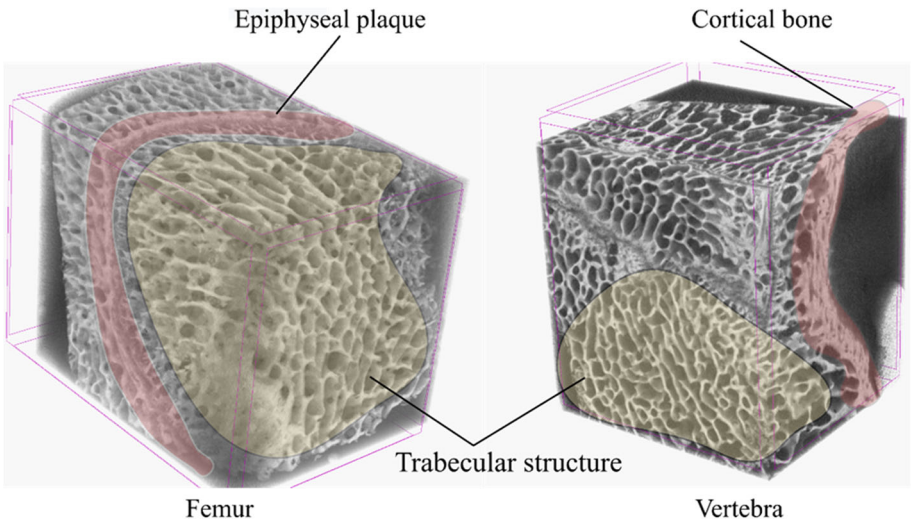

Fig. 1 Appearance of the internal structure of trabecular bones scanned by micro-CT

Table 1 SLM working parameters in detail

Laser parameter/region	Surface	Contours	Supports
Power (W)	200	200	100
Speed (mm/s)	1800	1250	650
Spot size (μm)	150	150	150

to generate 3D models of the samples cleaned after production. For Micro-CT, 9–12 μm image pixel size, 96–100 kV operational voltage, 100–104 mA current, and 0.11 mm Cu filter were used as its parameters. According to the obtained scanning data, the 3D CAD model creation process was the same as that of the bone. The Geomagic Control X™ software was used to align the pre-production trabecular structure and the postproduction model. Best fit alignment was used as the alignment method since all the geometries on the part and their positions with each other changed after production. In order to determine the deviations in the production after the alignment, two-dimensional sections were taken from the aligned CAD data, while the geometric changes in the building direction planes (X–Z and Y–Z) and the horizontal layer plane (X–Y) were examined.

2.2.2 Pore Network Models of Trabecular Structure

Pore network models (PNMs) were created from the CAD data of the trabecular bones and produced samples. The internal connection ratio and pore size distribution of both models could be obtained through the PNM. Avizo™ software was used for the creation of the PNM. By comparing the obtained PNMs, the deviations and ability of the produced trabecular structure representation of the bone were evaluated. In the PNM of the structure, the pores were defined as spherical geometry and the shape of the arms connecting the pores were defined as cylindrical [5].

In this study, the porous area was first defined and pore volumes were separated according to the model to be developed by the algorithm. PNM was then obtained by defining the cylindrical connecting arms and spherical pores (Fig. 2). The size, position, area, volume, and connection property values of the spherical and cylindrical representations from PNM can be reached. In this manner, the comparison of production and design was made possible, and the locations and dimensional distributions of closed pore defects in the structure were determined.

3 Results and Discussion

3.1 Trabecular Structure of Bone

Scanned and cross-sectional images obtained using Micro-CT on bone samples of a sheep are shown in Figs. 3 and 4, respectively. In 2D cross-sectional images, it was observed that the size and geometrical distributions of the cavities in the trabecular structure were irregular. The 3D CAD models of vertebra and femur were created from cross-sectional images to determine their structural properties. Figure 3 shows an example of a site-free selection of volumes in which the trabecular structure is disrupted (epiphyseal plaque, cortical bone, and areas of damaged bone). Generated cylindrical

Table 2 Ti6Al4V ELI chemical composition

Alloy element	Al	V	O	N	C	H	Fe	Ti
% Weight ratio	5.5–6.5	3.5–4.5	0–0.13	0–0.04	0–0.08	0–0.012	0–0.25	Balanced

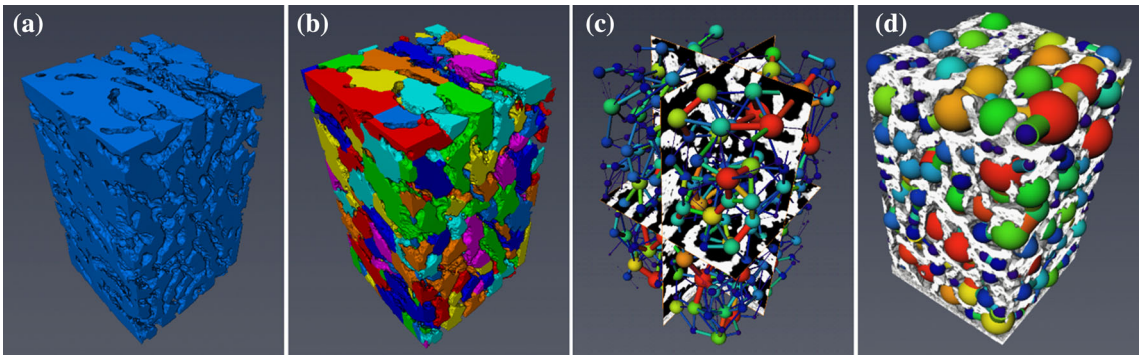

Fig. 2 PNM formation mechanism in Avizo™ software: **a** determination of pores in trabecular structure, **b** separation of pore volumes, **c** representation of pore network model by applying scale, and **d** PNM representation in trabecular structure

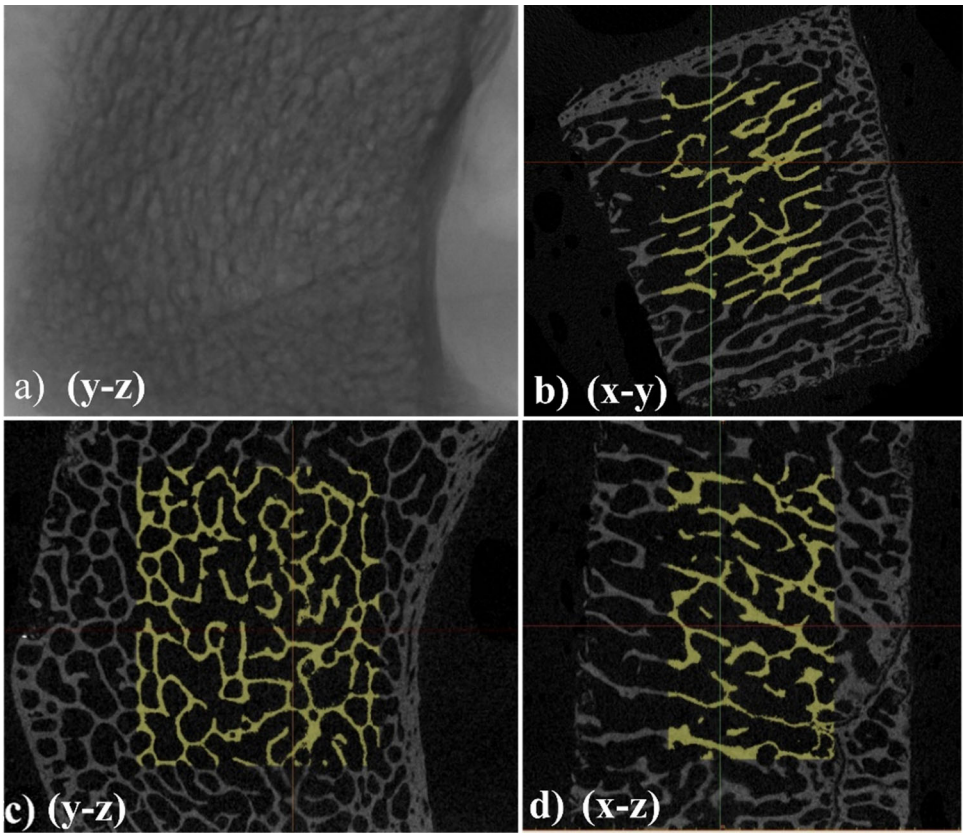

Fig. 3 Vertebra trabecular structure: **a** Micro-CT image and **b**–**d** cross sectional views with useful areas (yellow in color) for creating the 3D model of a sheep vertebra in different directions (created in Mimics software)

models created for the production of the bone are also shown in Fig. 5.

3D illustration of the pore network models of the bone is shown in Fig. 6. According to evaluations of the obtained pore network models, it was found that both the vertebra and the femur had 100% interconnected cavities for the natural development of marrow tissue and circulation. Dimensional distribution of the pores and the connecting arms was also determined and shown in Fig. 7. The equivalent spherical diameter of pores obtained from the sheep vertebra had a distribution between 102 and 1719 μm, and the average equivalent diameter of these pores was 767 ± 264 μm. When the dimensional distribution of the connecting arms in the vertebra was examined, the average equivalent cylindrical arm diameter was calculated as 305 ± 278 μm. The equivalent spherical diameters of the cavities of the sheep femur were also found to have a distribution between 90 and 1434 μm, and the average equivalent diameter was 624 ± 245 μm. When the dimensional distribution of the connecting arms in the femur was examined, the average diameter of the equivalent cylindrical arm was calculated as 248 ± 244 μm.

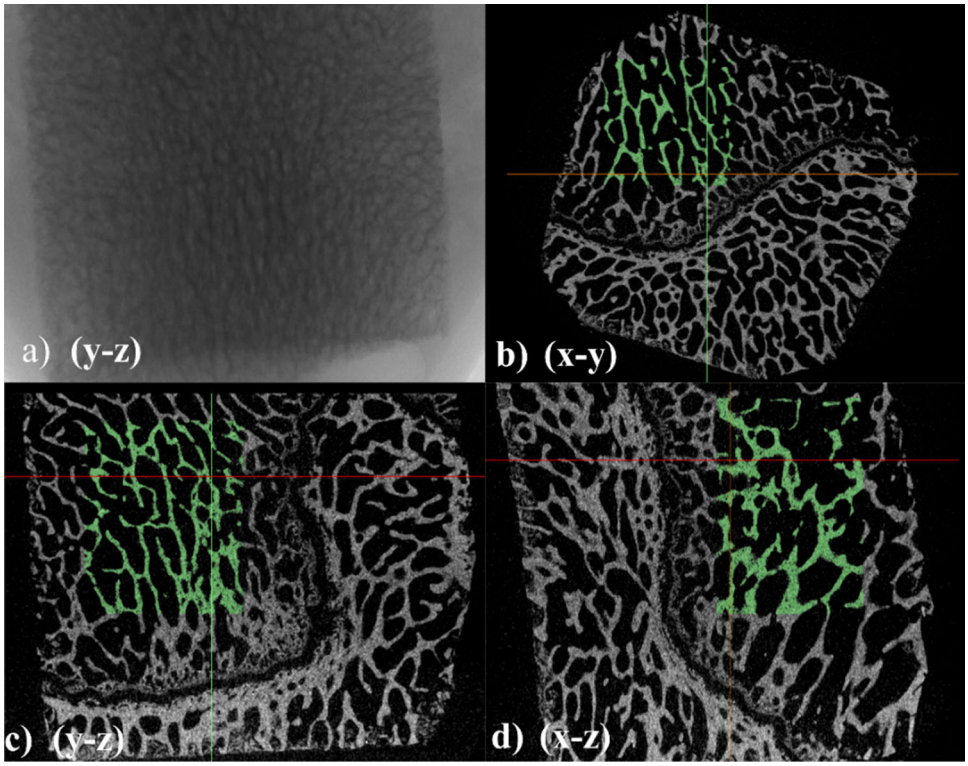

Fig. 4 Femur trabecular structure: **a** Micro-CT image and **b**–**d** cross sectional views with useful areas (green in color) for creating the 3D model of a sheep femur in different directions (created in Mimics software)

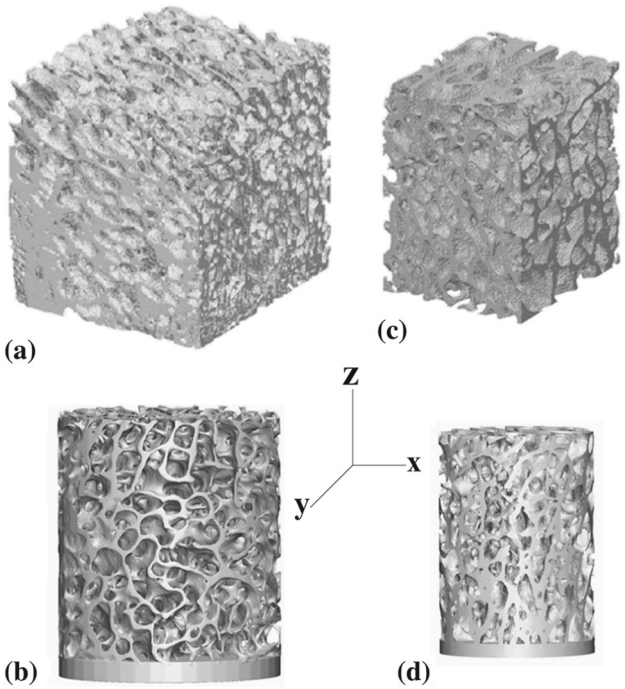

Fig. 5 Generated models: **a**, **b** bone model obtained from the vertebra and the model created for production, **c**, **d** bone model obtained from the femur and the model created for production

3.2 Analyses of the Samples by SLM

Trabecular bone geometries are produced by the SLM, and the appearances of the produced samples are depicted in Fig. 8. The samples were scanned by Micro-CT and ring artifact, and beam hardening defects were observed in the cross-sectional images (Fig. 9a). With the NRecon software, where cross-sectional images were created, beam hardening and ring artifact defects were removed and the images were improved (Fig. 9b).

Furthermore, by improving the cross-sectional images, unwanted pore defects remaining in the structure became apparent (Fig. 9b). From the improved cross-sectional views, 3D models of the structured geometries were created (Fig. 9a, b). The porosities were calculated and compared with the trabecular structure in the region where it was taken (Table 3). When the comparison was examined, it was concluded that the dimensions of the pores decreased. The porosity also decreased due to the increase in the size of trabecular arms. It was also found that both the porosity and pore dimensions increased with the increasing productional scale (Table 3). Due to the lower pore sizes in the femur trabecular structure, the percentage value of the geometry change caused by thickening and sagging was higher than the vertebral samples. For this reason, it was determined that the 1:1 scale porosity ratio of femoral samples had the lowest porosity ratio among the produced samples (Fig. 10).

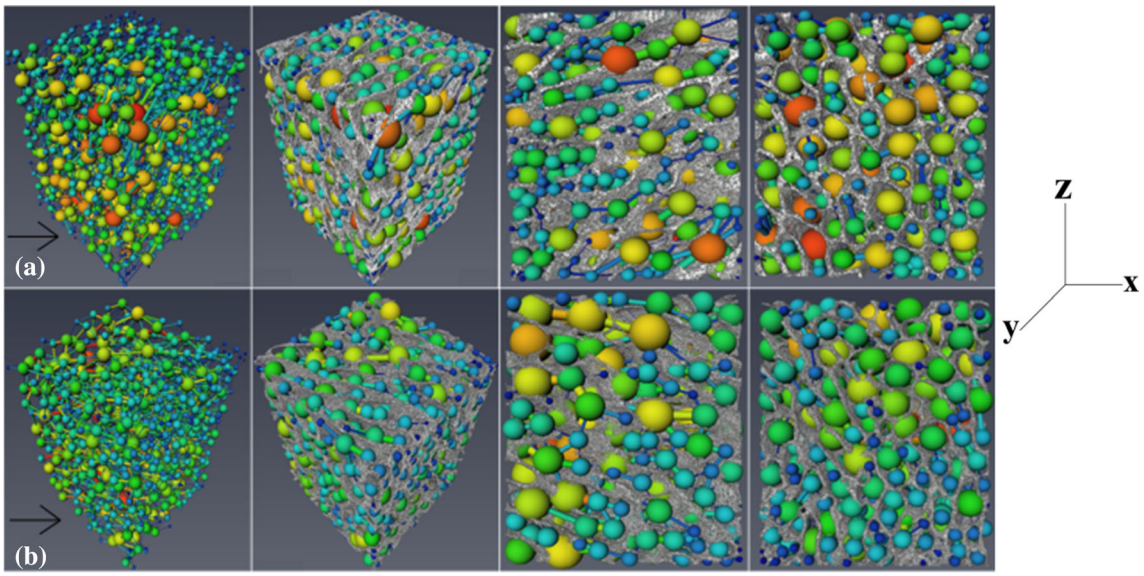

Fig. 6 Appearance of PNMs created using tomography data for **a** vertebra and **b** femur

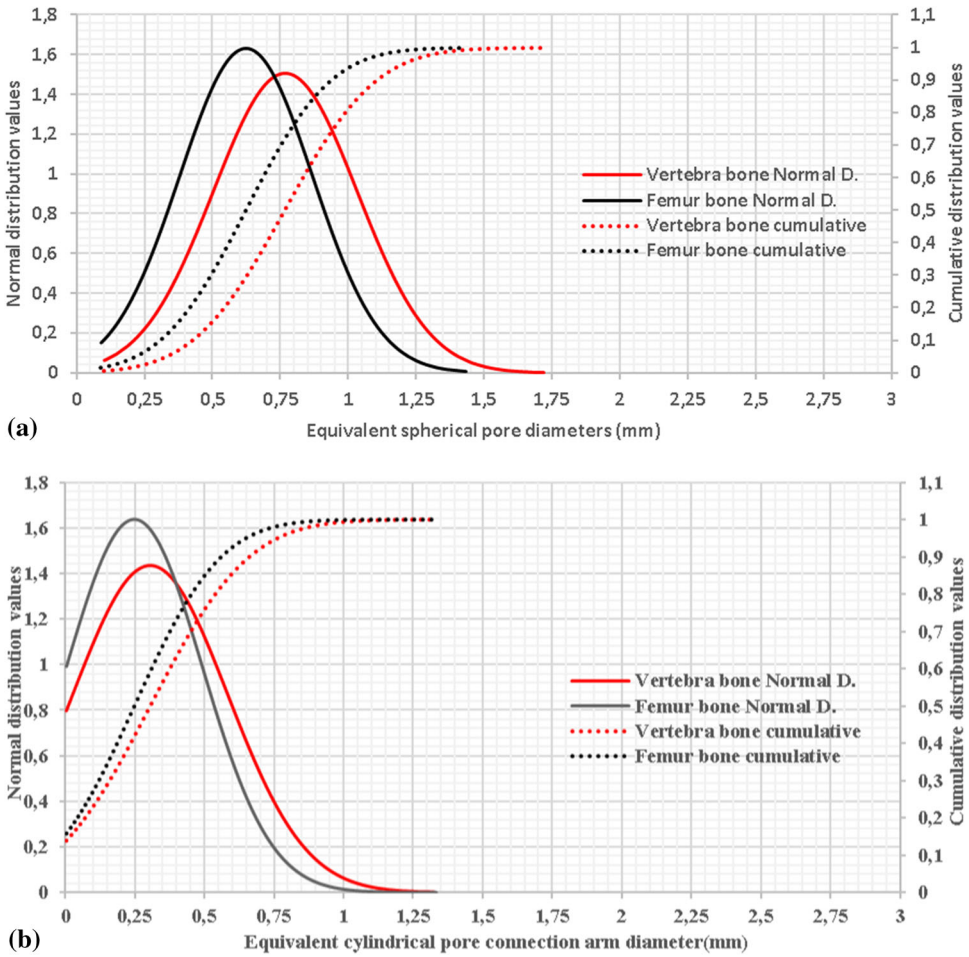

Fig. 7 Pore dimensional distributions obtained from PNMs: **a** equivalent diameter of pores and **b** equivalent diameter of connecting arms

With the help of the 3D data of postproduction and the alignment to pre-production geometry (Fig. 11a), 2D changes from the cross-sections of the production were examined (Fig. 11b, c). Thickness measurements were made before and after production by determining the angles of the trabecular cage in different cross-sectional images (Fig. 12). It

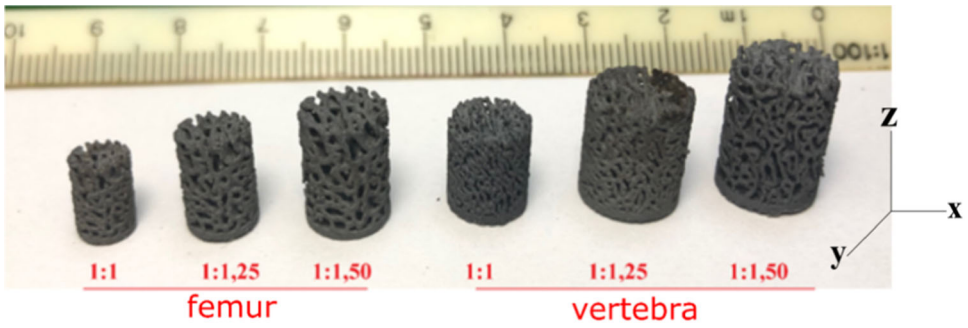

Fig. 8 Image of samples manufactured using SLM [59]

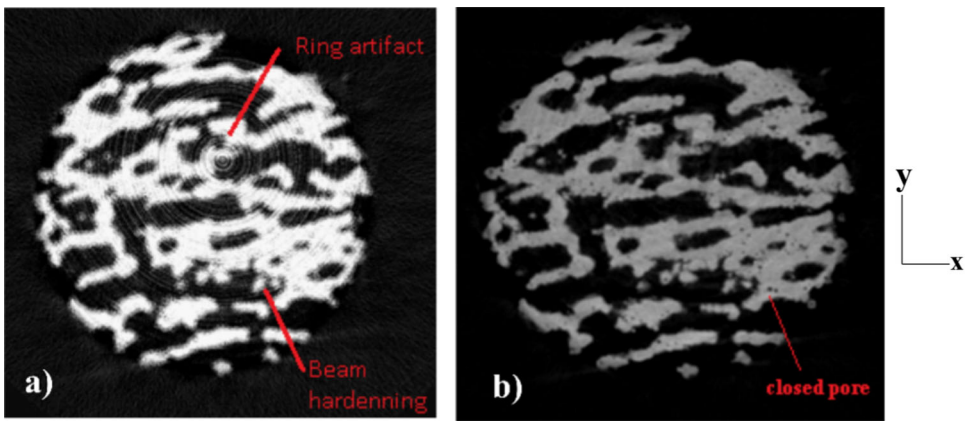

Fig. 9 Cross-sectional views of the model created from the SLMed vertebra by 1:1 scale obtained from Micro-CT: **a** image with defects, and **b** defect-free structural image

Table 3 Porosites of trabecular structures and SLMed samples [59]

	Vertebra			Femur		
Porosity of trabecular bone (%)	75			68		
Productional scale	1:1	1:1.25	1:1.50	1:1	1:1.25	1:1.50
Porosity of produced samples (%)	54,45	54,08	60,95	39,29	48,88	60,58

was determined that the change in the production increased by decreasing the arm angle. Dimensional deviations on the thicknesses of the arms perpendicular to the building plane were less, whereas the deviations on the horizontal arms increased due to sagging. It was observed that the unsupported structures were the main reason for the dimensional change that caused sagging.

In the results of the thickness deviations depending on the angle *(from vertical planes)*, the average of the geometrical difference (in mm) detected in 0 (horizontal) to 90 (vertical) degrees within 10-degree steps was obtained, then the regression curves were calculated for maximum, minimum, and mean values (Fig. 13). When the obtained curvatures were examined, it was observed that the change in production depending on the building angle differed in 3 regions as: 0–30° (1st zone), 30°–60° (2nd zone), and 60°–90° (3rd zone). In the first region, the deviation was the highest compared to the other two regions. The dimensional differences due to sagging increased significantly since no support was used. In the second region, with the increase of the arm angle from the building plane, the ability to support element geometry itself increased; therefore, the deviation decreased rapidly. In the third region, the dimensional deviation in production was measured as the lowest. The green region in Fig. 13 shows the standard deviation of the curvature of mean values.

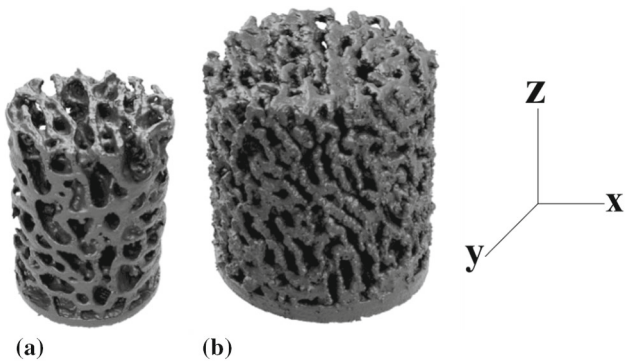

Fig. 10 Generated 3D models of SLMed samples: **a** 3D femur by 1:1 scale, and **b** 3D vertebra by 1:1 scale

In the measurements from the building slices (*from horizontal planes*), the laser spot diameter was considered 150

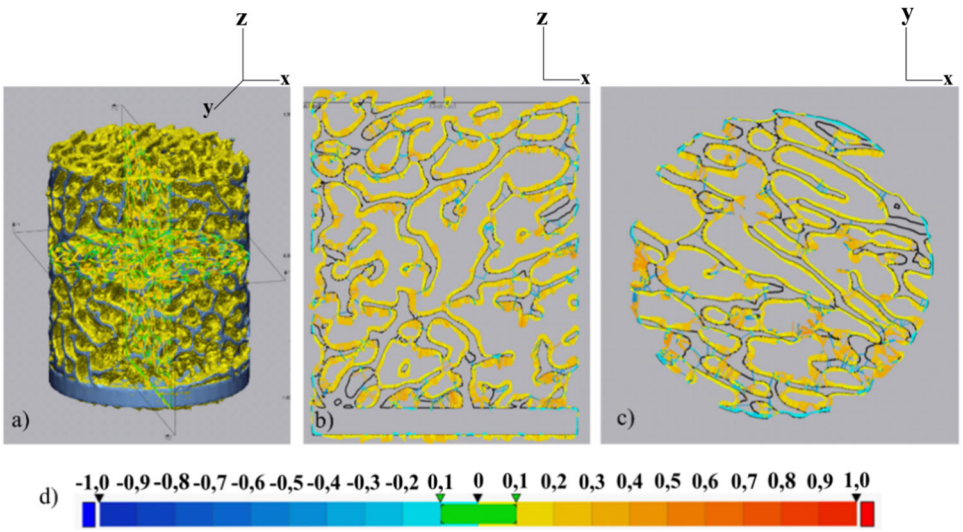

Fig. 11 **a** 3D aligned geometries, **b** differences in cross-sectional area parallel to the building direction, **c** differences in the plane parallel to the building layer, and **d** dimensional values of the differences on the color scale in mm

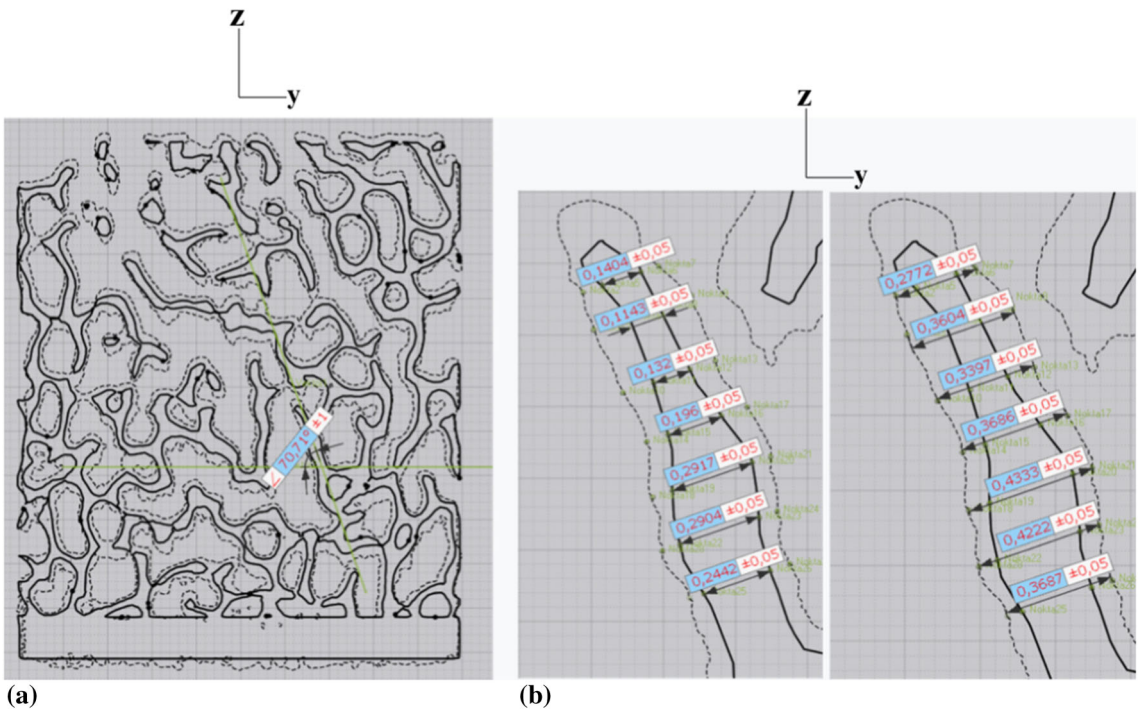

Fig. 12 Analysis of cross-sectional changes (picture is obtained from a vertebra with 1:1.25 scale): **a** determination of an element angle on the building direction and **b** thickness measurements in mm (-----SLMed part and ——trabecular bone)

micron in order to calculate the average deviation on the thicknesses of the trabecular arms which was below and above 150 micron. In the case where the arm thickness was below 150 micron, the average deviation was measured as 236%, whereas when it was over 150 micron, the average deviation was 70%. It is concluded that the deviation will be considerably high when the thickness is below than when the spot diameter on the building slices the plane horizontally.

Considering the literature studies, it is accepted that the distribution is normal when the skewness value of a distribution is between − 1.5 and + 1.5 and the kurtosis value is between − 1 and + 1 [60, 61]. It has been determined that the calculated skewness and kurtosis values of the PNM pore and connecting arm size distributions are suitable for these conditions and have a normal distribution (Table 4). The distribution of pore and connection arm diameters obtained from the network models created is given in Figs. 7 and 14.

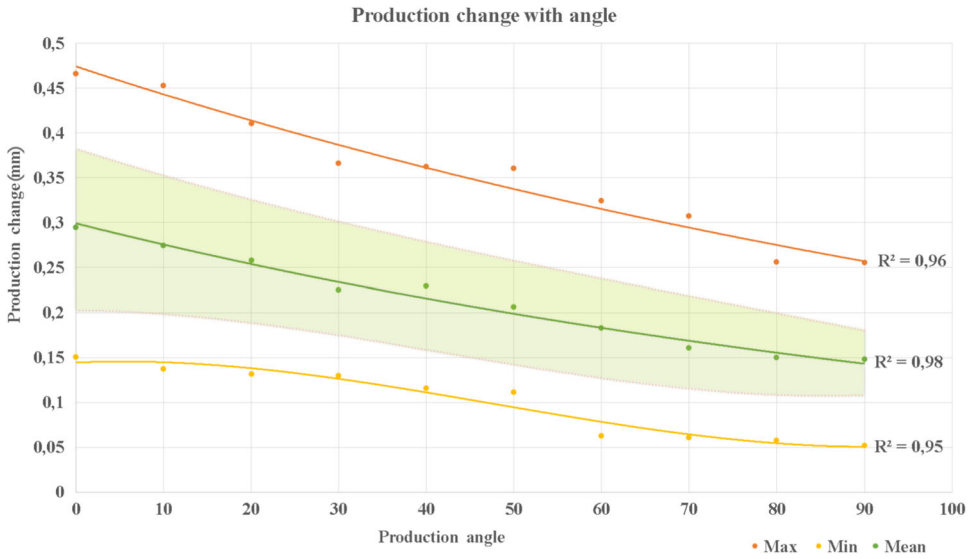

Fig. 13 Average deviation of thickness on the inclined arms

From the pore network models on both bones and produced samples, the internal connection rate of the trabecular structures was 100%. It was observed that the equivalent diameter of the trabecular pores and the produced 1:1 scaled samples were close to each other both in the smallest and largest diameters (Fig. 4a, d). Furthermore, it was discovered that the diameter dimensions of the pore equivalent in the structure naturally increased by increasing the production scale. Additionally, when the distribution values of lattice connection arm diameters were examined, it was concluded that the productions to be made between 1: 1 and 1: 1.25 scales would have similar dimensional distribution values with trabecular bone (Fig. 14).

It was determined that the mean diameter values of natural vertebra and femur trabecular structures copied from sheep bone for porous structure production varied between 767 ± 264 and 624 ± 245 μm (Table 4). It was observed that the detected pore range is compatible with direct bone formation over 300 μm [19] and a pore size of 1000 μm where high cell density and metabolic activity are detected [62, 63], and current studies were shown to be compatible with the natural bone structure. The lower limit of pore size was 102 μm and 90 μm for vertebra, and femur was compatible with the absence of blood in pores with a size less than 50 μm and even limited to 90 μm. The highest pore value examined in literature studies and found to be suitable for bone adaptation is 1220 μm [5, 64] and it was observed that the replicated natural sheep trabecular structure had a pore size of 1718 μm in the vertebra and 1434 μm in the femur for tissue development.

In this study, the geometry of the closed pores and their distribution within the structure, as well as the open pores, were examined with the PNM technique. It was determined that the closed spaces spread throughout the building elements and the spherical equivalent diameter of the size distribution was 51 ± 29 μm and closed spaces up to 288 μm equivalent diameter were formed in the production (Fig. 15). Although the geometries of the closed pore volumes are close to the spherical geometry throughout the structure, a small amount of v-shaped pores was formed in the structure. The pore shape formed in the production with SLM was caused by the recoil pressure and surface tension in the melting pool [65]. In addition, the energy density, temperature distribution and cooling rate used in production for melting are effective in the positioning of the pores [66–68]. High recoil pressure occurs as a result of the sudden increase in temperature in the laser effect area with laser pulse and reflections in the powder bed. The surface tension decreases and metal vapor occurs with the increase in temperature [69]. As in EBM productions, in SLM productions made with high energy input, metal vapor, or gas that is trapped inside creates a spherical-shaped pore geometry with low surface tension [51, 67, 69]. However, in cases where the energy density is not sufficient for proper melting, the surface tension is higher than the recoil pressure and the upper layer with a high cooling rate solidifies rapidly due to low energy density, so the remaining gases cause the formation of v-shaped or sharp cracks in the shape of the melting pool [51, 69]. When the formation mechanisms are examined, it is concluded that the spherical closed space (pore) geometries observed throughout the structure are due to the high energy input (Fig. 16). The melt scattering observed during the production of the v-shaped pores, which are relatively small compared to the spherical pore, due to the local decrease in energy density as a result of shadowing laser beam radiation.

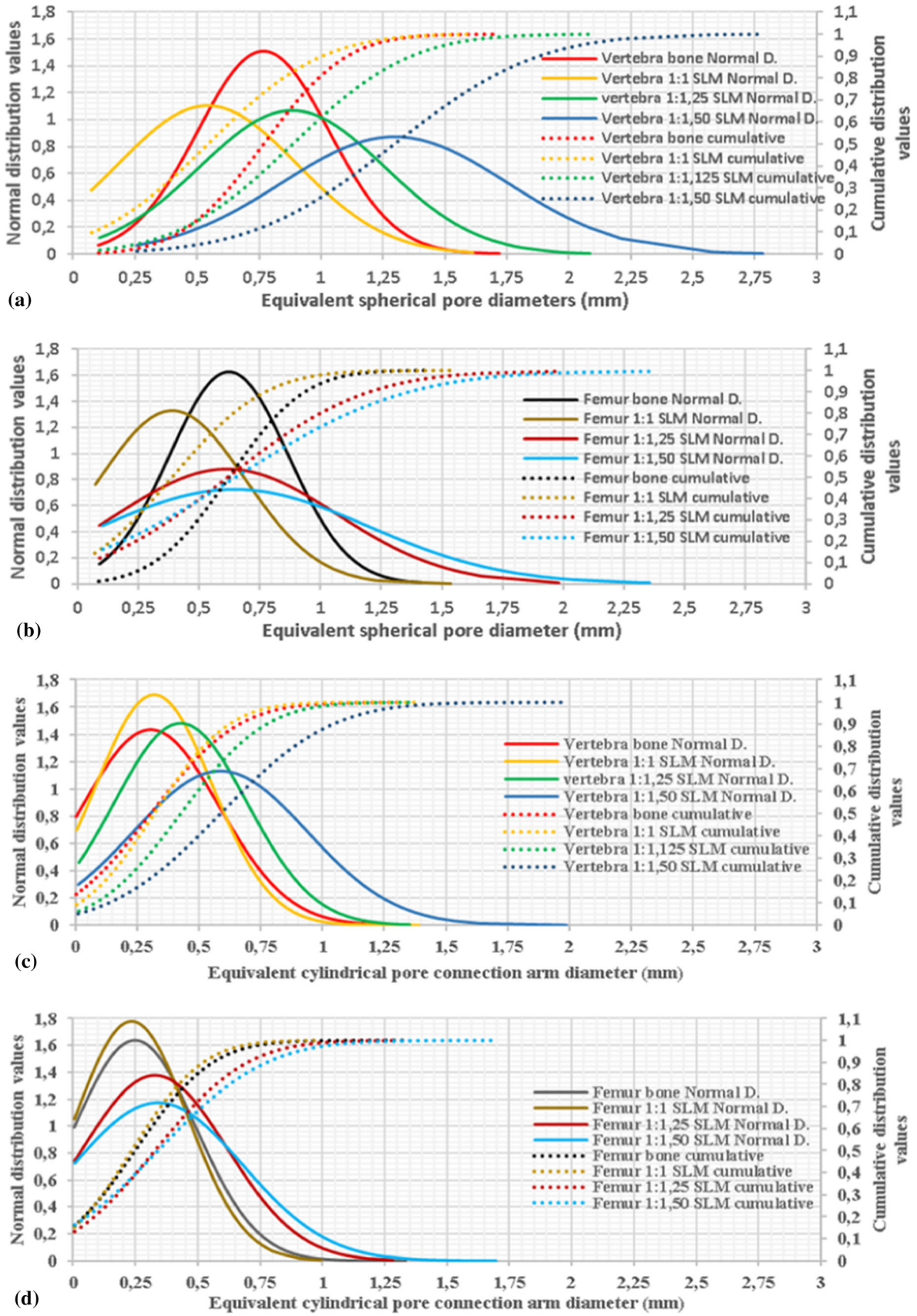

Fig. 14 Dimensional comparison of bone structure and pore network models produced by SLM: **a** equivalent pore diameters of the vertebra, **b** equivalent diameter of the cylindrical connecting arms of the vertebra, **c** equivalent pore diameter of the femur, and **d** equivalent diameter of the cylindrical connecting arms of femur

Table 4 The values of the distribution of pore and connecting arm diameters from PNM's

	Vertebra bone	Vertebra 1:1 SLM	Vertebra 1:1,25 SLM	Vertebra 1:1,50 SLM	Femur bone	Femur 1:1 SLM	Femur 1:1,25 SLM	Femur 1:1,5 SLM
Equivalent spherical pore diameters (mm)								
Average	0.767	0.544	0.885	1.297	0.623	0.390	0.616	0.647
Standard deviation	0.265	0.361	0.374	0.456	0.245	0.300	0.452	0.553
Variance	0.070	0.131	0.140	0.208	0.060	0.090	0.205	0.306
Skewness	0.303	0.222	0.073	0.423	0.319	0.744	0.515	0.813
Kurtosis	− 0.003	− 0.915	− 0.163	0.462	− 0.220	− 0.223	− 0.809	− 0.412
Min	0.103	0.075	0.107	0.257	0.090	0.074	0.091	0.104
Max	1.719	1.616	2.088	2.783	1.434	1.538	1.980	2.356
Equivalent cylindrical pore connection arm diameters (mm)								
Average	0.305	0.319	0.426	0.587	0.248	0.234	0.328	0.341
Standart deviation	0.278	0.236	0.269	0.353	0.244	0.224	0.290	0.340
Variance	0.077	0.056	0.072	0.124	0.059	0.050	0.084	0.116
Skewness	0.839	0.712	0.633	0.499	1.137	0.949	0.902	1.121
Kurtosis	− 0.237	0.110	− 0.068	− 0.187	0.449	− 0.005	− 0.046	0.504
Min	0.004	0.005	0.015	0.012	0.004	0.005	0.005	0.006
Max	1.324	1.391	1.353	1.988	1.333	0.996	1.282	1.697

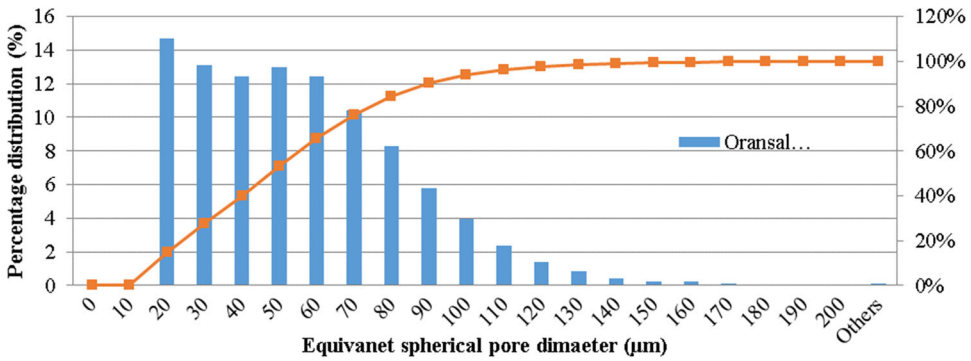

Fig. 15 Equivalent diameter distribution of undesirable pores in produced samples

4 Conclusion

In this study, the reproducibility of the trabecular bone structures of a sheep was investigated. For this purpose, the samples were taken from the vertebra and femur region of the sheep and scanned using Micro-CT. The Micro-CT of trabecular structures was then produced by the SLM. The samples from SLM were scanned by Micro-CT, and 3D models were obtained. Differences were determined by aligning the geometries before and after the production. In addition, the PNMs of the samples obtained from the bones and produced samples were created. Size distribution of the pores and the internal connection ratio were examined on PNMs. The results of the study are as follows.

- As the arm angle in trabecular structures increased (when the arms got closer to the vertical), the amount of deviation decreased. Even if the angle of inclined arms was vertical, a deviation of at least 150 microns was observed.
- As the thickness increased, the fluctuation on deviation decreased independently from the arm angle. Particularly, the production of trabecular arms below 150 microns was found to accelerate the deviation.
- The thickness below 300 micron caused a difficulty in production due to the minimum spot size of the laser and deviations.
- As the scale of the model increased, the thickness of the arms in the model also increased. With increasing arm thickness, the deviation decreased and porosity ratio increased.
- The internal connection ratios of both the trabecular structure and SLM samples obtained from PNMs were found to be 100%, and the bone structure was successfully imitated

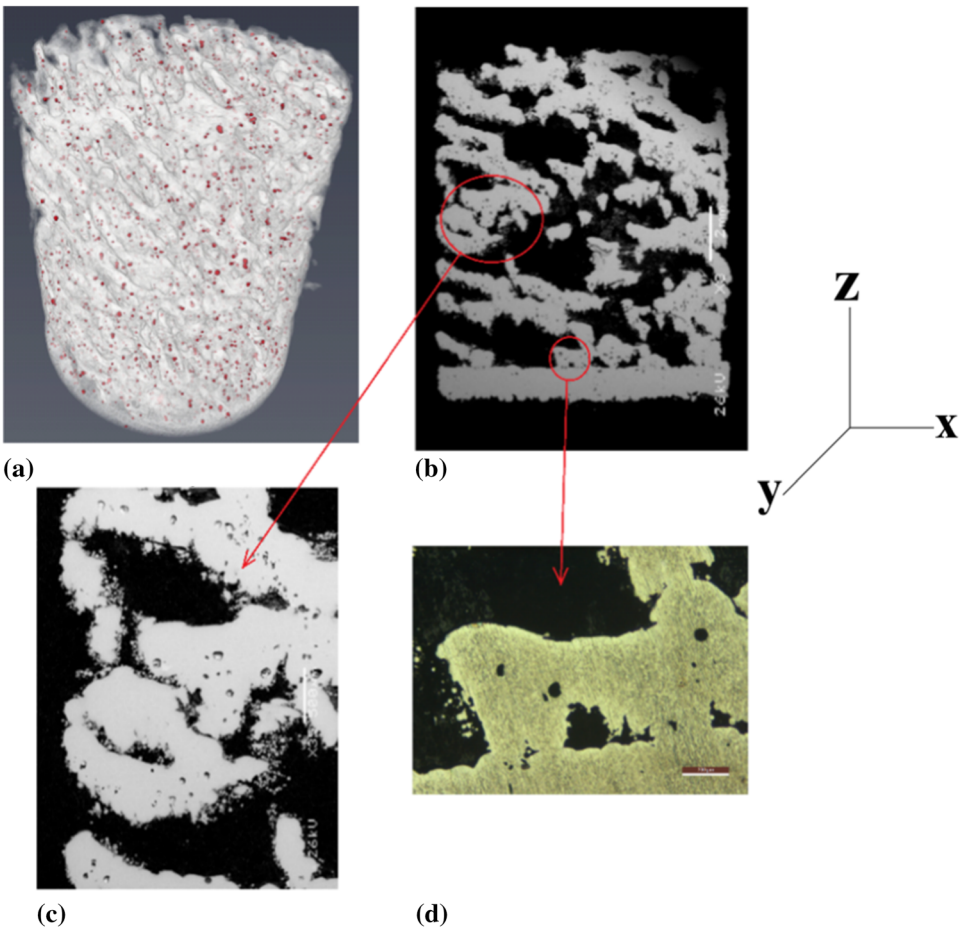

Fig. 16 Representation of undesirable pores: **a** Pore distribution from PNM in the vertebra 1:1 scale, **b** and **c** scanning electron microscopy images, and **d** optical microscope images

between 1:1 and 1:1.25 productional scales, which proved that the samples produced by imitating the bone.

Acknowledgments This study is supported by Gazi University as a Scientific Research Project with number 06/2018-11. This study is supported by Gülhane Medical Design and Production Center for modeling and production. Authors thank EKTAM (Additive Manufacturing Technology Application and Research Center) for their support.

References

1. Hing, K.A.; Best, S.M.; Bonfield, W.: Characterization of porous hydroxyapatite. *J. Mater. Sci. Mater. Med.* **10**(3), 135–145, 1999
2. Billiet, T.; Gevaert, E.; De Schryver, T.; Cornelissen, M.; Dubruel, P.: The 3D printing of gelatinmethacrylamide cell-laden tissue-engineered constructs with high cell viability. *Biomaterials* **35**(1), 49–62, 2014
3. Mooney, D.J.; Sano, K.; Matthias Kaufmann, P.; Majahod, K.; Schloo, B.; Vacanti, J.P.; et al.: Long-term engraftment of hepatocytes transplanted on biodegradable polymer sponges. *J. Biomed. Mater. Res.* **37**(3), 413–420, 1997
4. Hurtado, A.; Moon, L.D.F.; Maquet, V.; Blits, B.; Jérôme, R.; Oudega, M.: Poly (d,l-lactic acid) macroporous guidance scaffolds seeded with Schwann cells genetically modified to secrete a bi-functional neurotrophin implanted in the completely transected adult rat thoracic spinal cord. *Biomaterials* **27**(3), 430–442, 2006
5. Jones, A.C.; Arns, C.H.; Hutmacher, D.W.; Milthorpe, B.K.; Sheppard, A.P.; Knackstedt, M.A.: The correlation of pore morphology, interconnectivity and physical properties of 3D ceramic scaffolds with bone ingrowth. *Biomaterials* **30**(7), 1440–1451, 2009
6. Currey, J.D.: Bones: structure and mechanics, pp. 5–456. Princeton University Press, Princeton (2006)
7. Bose, S.; Vahabzadeh, S.; Bandyopadhyay, A.: Bone tissue engineering using 3D printing. *Mater. Today* **16**(12), 496–504, 2013
8. Wang, X.; Xu, S.; Zhou, S.; Xu, W.; Leary, M.; Choong, P.; et al.: Topological design and additive manufacturing of porous metals for bone scaffolds and orthopaedic implants: a review. *Biomaterials* **83**, 127–141, 2016
9. Hutmacher, D.W.: Scaffolds in tissue engineering bone and cartilage. *Biomaterials* **21**(24), 2529–2543, 2000
10. Ponader, S.; von Wilmowsky, C.; Widenmayer, M.; Lutz, R.; Heinl, P.; Körner, C.; et al.: In vivo performance of selective electron beam-melted Ti–6Al–4V structures. *J. Biomed. Mater. Res. Part A* **92**(1), 56–62, 2010
11. Palmquist, A.; Emanuelsson, L.; Thomsen, P.; Palmquist, A.; Snis, A.; Emanuelsson, L.; et al.: Long-term biocompatibility and osseointegration of electron beam melted, free-form-fabricated solid and porous titanium alloy: experimental studies in sheep. *J. Biomater. Appl.* **27**(8), 1003–1016, 2013
12. Murr, L.E.: Open-cellular metal implant design and fabrication for biomechanical compatibility with bone using electron beam melting. *J. Mech. Behav. Biomed. Mater.* **76**, 164–177, 2017
13. Li, X.; Chu, C.; Zhou, L.; Bai, J.; Guo, C.; Xue, F.; et al.: Fully degradable PLA-based composite reinforced with 2D-braided Mg

wires for orthopedic implants. *Compos. Sci. Technol.* **142**, 180–188, 2017
14. Al-Tamimi, A.A.; Peach, C.; Fernandes, P.R.; Cseke, A.; Bartolo, P.J.D.S.: Topology optimization to reduce the stress shielding effect for orthopedic applications. *Procedia CIRP* **65**, 202–206, 2017
15. Tan, X.P.; Tan, Y.J.; Chow, C.S.L.; Tor, S.B.; Yeong, W.Y.: Metallic powder-bed based 3D printing of cellular scaffolds for orthopaedic implants: a state-of-the-art review on manufacturing, topological design, mechanical properties and biocompatibility. *Mater. Sci. Eng. C* **76**, 1328–1343, 2017
16. Zaharin, H.A.; Abdul Rani, A.M.; Azam, F.I.; Ginta, T.L.; Sallih, N.; Ahmad, A.; et al.: Effect of unit cell type and pore size on porosity and mechanical behavior of additively manufactured Ti6Al4V scaffolds. *Materials* **11**(12), 2402, 2018
17. Wang, Y.; Arabnejad, S.; Tanzer, M.; Pasini, D.: Hip implant design with three-dimensional porous architecture of optimized graded density. *J. Mech. Des.* **140**(11), 111406, 2018
18. Itälä, A.I.; Ylänen, H.O.; Ekholm, C.; Karlsson, K.H.; Aro, H.T.: Pore diameter of more than 100 μm is not requisite for bone ingrowth in rabbits. *J. Biomed. Mater. Res. Off. J. Soc. Biomater. Jpn. Soc. Biomater. Aust. Soc. Biomater. Korean Soc. Biomater.* **58**(6), 679–683, 2001
19. Kuboki, Y.; Jin, Q.; Takita, H.: Geometry of carriers controlling phenotypic expression in BMP-induced osteogenesis and chondrogenesis. *JBJS* **83**(1), 105–115, 2001
20. Structure of Bones|Biology for MajorsI. https://courses.lumenlearning.com/wmbiology2/chapter/structure-of-bones/. Access date: 16 Nisan 2019
21. Tsuruga, E.; Takita, H.; Itoh, H.; Wakisaka, Y.; Kuboki, Y.: Pore size of porous hydroxyapatite as the cell-substratum controls BMP-induced osteogenesis. *J. Biochem.* **121**(2), 317–324, 1997
22. de Wild, M.; Zimmermann, S.; Rüegg, J.; Schumacher, R.; Fleischmann, T.; Ghayor, C.; et al.: Influence of microarchitecture on osteoconduction and mechanics of porous titanium scaffolds generated by selective laser melting. *3D Print. Addit. Manuf.* **3**(3), 142–151, 2016
23. Rouwkema, J.; Rivron, N.C.; van Blitterswijk, C.A.: Vascularization in tissue engineering. *Trends Biotechnol.* **26**(8), 434–441, 2008
24. Kumar, A.; Nune, K.C.; Murr, L.E.; Misra, R.D.K.: Biocompatibility and mechanical behaviour of three-dimensional scaffolds for biomedical devices: process-structure-property paradigm. *Int. Mater. Rev.* **61**(1), 20–45, 2016
25. Eli, T.: Relationship between unit cell type and porosity and the fatigue behavior of selective laser melted. *J. Mech. Behav. Biomed. Mater.* **43**, 91–100, 2015
26. Ahmadi, S.M.; Yavari, S.A.; Wauthle, R.; Pouran, B.; Schrooten, J.; Weinans, H.; Zadpoor, A.A.: Additively manufactured open-cell porous biomaterials made from six different space-filling unit cells: the mechanical and morphological properties. *Materials* **8**(4), 1871–1896, 2015
27. Wieding, J.; Wolf, A.; Bader, R.: Numerical optimization of open-porous bone scaffold structures to match the elastic properties of human cortical bone. *J. Mech. Behav. Biomed. Mater.* **37**, 56–68, 2014
28. Parthasarathy, J.; Starly, B.; Raman, S.; Christensen, A.: Mechanical evaluation of porous titanium (Ti6Al4V) structures with electron beam melting (EBM). *J. Mech. Behav. Biomed. Mater.* **3**(3), 249–259, 2010
29. Wauthle, R.; Van Der Stok, J.; Yavari, S.A.; Van Humbeeck, J.; Kruth, J.P.; Zadpoor, A.A.; et al.: Additively manufactured porous tantalum implants. *ActaBiomater.* **14**, 217–225, 2015
30. Kadkhodapour, J.; Montazerian, H.; Darabi, A.C.; Anaraki, A.P.; Ahmadi, S.M.; Zadpoor, A.A.; et al.: Failure mechanisms of additively manufactured porous biomaterials: effects of porosity and type of unit cell. *J. Mech. Behav. Biomed. Mater.* **50**, 180–191, 2015
31. Wauthle, R.; Vrancken, B.; Beynaerts, B.; Jorissen, K.; Schrooten, J.; Kruth, J.P.; et al.: Effects of build orientation and heat treatment on the microstructure and mechanical properties of selective laser melted Ti6Al4V lattice structures. *Addit. Manuf.* **5**, 77–84, 2015
32. Arabnejad, S.; Burnett Johnston, R.; Pura, J.A.; Singh, B.; Tanzer, M.; Pasini, D.: High-strength porous biomaterials for bone replacement: a strategy to assess the interplay between cell morphology, mechanical properties, bone ingrowth and manufacturing constraints. *ActaBiomater.* **30**, 345–356, 2016
33. Fantini, M.; Curto, M.; De Crescenzio, F.: A method to design biomimetic scaffolds for bone tissue engineering based on Voronoi lattices. *Virtual Phys. Prototyp.* **11**(2), 77–90, 2016
34. Liang, H.; Yang, Y.; Xie, D.; Li, L.; Mao, N.; Wang, C.; et al.: Trabecular-like Ti–6Al–4V scaffolds for orthopedic: fabrication by selective laser melting and in vitro biocompatibility. *J. Mater. Sci. Technol.* **35**(7), 1284–1297, 2019
35. Barak, M.M.; Black, M.A.: A novel use of 3D printing model demonstrates the effects of deteriorated trabecular bone structure on bone stiffness and strength. *J. Mech. Behav. Biomed. Mater.* **78**, 455–464, 2018
36. Wood, Z.; Lynn, L.; Nguyen, J.T.; Black, M.A.; Patel, M.; Barak, M.M.: Are we crying Wolff? 3D printed replicas of trabecular bone structure demonstrate higher stiffness and strength during off-axis loading. *Bone* **127**, 635–645, 2019
37. Cheng, A.; Humayun, A.; Cohen, D.J.; Boyan, B.D.; Schwartz, Z.: Additively manufactured 3D porous Ti–6Al–4V constructs mimic trabecular bone structure and regulate osteoblast proliferation, differentiation and local factor production in a porosity and surface roughness dependent manner. *Biofabrication* **6**(4), 1–12, 2014
38. Shipley, H.; McDonnell, D.; Culleton, M.; Coull, R.; Lupoi, R.; O'Donnell, G.; et al.: Optimisation of process parameters to address fundamental challenges during selective laser melting of Ti–6Al–4V: a review. *Int. J. Mach. Tools Manuf.* **128**, 1–20, 2018
39. Attar, H.; Calin, M.; Zhang, L.C.C.; Scudino, S.; Eckert, J.: Manufacture by selective laser melting and mechanical behavior of commercially pure titanium. *Mater. Sci. Eng. A* **593**, 170–177, 2014
40. Liu, L.; Kamm, P.; García-Moreno, F.; Banhart, J.; Pasini, D.: Elastic and failure response of imperfect three-dimensional metallic lattices: the role of geometric defects induced by Selective Laser Melting. *J. Mech. Phys. Solids* **107**, 160–184, 2017
41. Bagheri, Z.S.; Melancon, D.; Liu, L.; Johnston, R.B.; Pasini, D.: Compensation strategy to reduce geometry and mechanics mismatches in porous biomaterials built with selective laser melting. *J. Mech. Behav. Biomed. Mater.* **70**, 17–27, 2017
42. Bael, S.V.; Kerckhofs, G.; Moesen, M.; Pyka, G.; Schrooten, J.; Kruth, J.P.: Micro-CT-based improvement of geometrical and mechanical controllability of selective laser melted Ti6Al4V porous structures. *Mater. Sci. Eng. A* **528**(24), 7423–7431, 2011
43. Mazur, M.; Leary, M.; McMillan, M.; Sun, S.; Shidid, D.; Brandt, M.: Mechanical properties of Ti6Al4V and AlSi12Mg lattice structures manufactured by selective laser melting (SLM). In: Brandt, M. (ed.) Laser Additive Manufacturing: Materials, Design, Technologies, and Applications, Chap. 5, pp. 119–161, 1st edn. Elsevier Science & Technology (2016). https://doi.org/10.1016/B978-0-08-100433-3.00005-1
44. Gu, D.; Hagedorn, Y.-C.; Meiners, W.; Meng, G.; Batista, R.J.S.; Wissenbach, K.; et al.: Densification behavior, microstructure evolution, and wear performance of selective laser melting processed commercially pure titanium. *Acta Mater.* **60**(9), 3849–3860, 2012
45. Leuders, S.; Thöne, M.; Riemer, A.; Niendorf, T.; Tröster, T.; Richard, H.A.A.; et al.: On the mechanical behaviour of titanium alloy TiAl6V4 manufactured by selective laser melting: fatigue resistance and crack growth performance. *Int. J. Fatigue* **48**, 300–307, 2013
46. Murr, L.E.; Quinones, S.A.; Gaytan, S.M.; Lopez, M.I.; Rodela, A.; Martinez, E.Y.; et al.: Microstructure and mechanical behavior of

Ti–6Al–4V produced by rapid-layer manufacturing, for biomedical applications. *J. Mech. Behav. Biomed. Mater.* **2**(1), 20–32, 2009
47. Murr, L.E.; Esquivel, E.V.; Quinones, S.A.; Gaytan, S.M.; Lopez, M.I.; Martinez, E.Y.; et al.: Microstructures and mechanical properties of electron beam-rapid manufactured Ti–6Al–4V biomedical prototypes compared to wrought Ti–6Al–4V. *Mater. Charact.* **60**(2), 96–105, 2009
48. Vilaro, T.; Colin, C.; Bartout, J.D.: As-fabricated and heat-treated microstructures of the Ti–6Al–4V alloy processed by selective laser melting. *Metall. Mater. Trans. A* **42**(10), 3190–3199, 2011
49. Thijs, L.; Verhaeghe, F.; Craeghs, T.; Humbeeck, J.V.; Kruth, J.-P.P.: A study of the microstructural evolution during selective laser melting of Ti–6Al–4V. *Acta Mater.* **58**(9), 3303–3312, 2010
50. Attar, H.; Bönisch, M.; Calin, M.; Zhang, L.-C.; Scudino, S.; Eckert, J.: Selective laser melting of in situ titanium–titanium boride composites: processing, microstructure and mechanical properties. *Acta Mater.* **76**, 13–22, 2014
51. Kasperovich, G.; Haubrich, J.; Gussone, J.; Requena, G.: Correlation between porosity and processing parameters in TiAl6V4 produced by selective laser melting. *Mater. Des.* **105**, 160–170, 2016
52. Tobergte, D.R.; Curtis, S.: Defect morphology in Ti–6AL–4V parts fabricated by selective laser melting and electron beam melting. *J. Chem. Inf. Model.* **53**(9), 1689–1699, 2013
53. Pang, S.; Chen, W.; Wang, W.: A quantitative model of keyhole instability induced porosity in laser welding of titanium alloy. *Metall. Mater. Trans. A* **45**(6), 2808–2818, 2014
54. Yang, J.; Han, J.; Yu, H.; Yin, J.; Gao, M.; Wang, Z.; et al.: Role of molten pool mode on formability, microstructure and mechanical properties of selective laser melted Ti–6Al–4V alloy. *Mater. Des.* **110**, 558–570, 2016
55. Courtois, M.; Carin, M.; Masson, P.L.; Gaied, S.; Balabane, M.: A new approach to compute multi-reflections of laser beam in a keyhole for heat transfer and fluid flow modelling in laser welding. *J. Phys. D Appl. Phys.* **46**(50), 505305, 2013
56. Qiu, C.; Adkins, N.J.E.E.; Attallah, M.M.: Microstructure and tensile properties of selectively laser-melted and of HIPed laser-melted Ti–6Al–4V. *Mater. Sci. Eng. A* **578**, 230–239, 2013
57. Stef, J.; Poulon-Quintin, A.; Redjaimia, A.; Ghanbaja, J.; Ferry, O.; De Sousa, M.; et al.: Mechanism of porosity formation and influence on mechanical properties in selective laser melting of Ti–6Al–4V parts. *Mater. Des.* **156**, 480–493, 2018
58. Voisin, T.; Calta, N.P.; Khairallah, S.A.; Forien, J.B.; Balogh, L.; Cunningham, R.W.; et al.: Defects-dictated tensile properties of selective laser melted Ti–6Al–4V. *Mater. Des.* **158**, 113–126, 2018
59. Küçükaltun, F.: Production of replicated trabecular bone structure by selective laser melting method using Ti6Al4V powder and observation of geometric accuracy, Master thesis, Gazi University, Ankara (2019)
60. George, D.; Mallery, M.: SPSS for Windows Step by Step: A Simple Guide and Reference, pp. 112–120. Allyn & Bacon, Boston (2010)
61. Tabachnick, B.G.; Fidell, L.S.; Ullman, J.B.: Using Multivariate Statistics, pp. 99–167. Pearson, Boston (2007)
62. N Taniguchi S Fujibayashi M Takemoto K Sasaki B Otsuki T Nakamura 2016 Effect of pore size on bone ingrowth into porous titanium implants fabricated by additive manufacturing: an in vivo experiment Mater. Sci. Eng. C 59:690 701
63. Van Bael, S.; Chai, Y.C.; Truscello, S.; Moesen, M.; Kerckhofs, G.; Van Oosterwyck, H.; et al.: The effect of pore geometry on the in vitro biological behavior of human periosteum-derived cells seeded on selective laser-melted Ti6Al4V bone scaffolds. *ActaBiomater.* **8**(7), 2824–2834, 2012
64. von Doernberg, M.-C.; von Rechenberg, B.; Bohner, M.; Grünenfelder, S.; van Lenthe, G.H.; Müller, R.; et al.: In vivo behavior of calcium phosphate scaffolds with four different pore sizes. *Biomaterials* **27**(30), 5186–5198, 2006
65. Geiger, M.; Leitz, K.H.; Koch, H.; Otto, A.: A 3D transient model of keyhole and melt pool dynamics in laser beam welding applied to the joining of zinc coated sheets. *Prod. Eng. Res. Dev.* **3**(2), 127–136, 2009
66. Gong, H.; Rafi, K.; Gu, H.; Janaki Ram, G.D.D.; Starr, T.; Stucker, B.: Influence of defects on mechanical properties of Ti–6Al–4V components produced by selective laser melting and electron beam melting. *Mater. Des.* **86**, 545–554, 2015
67. Pang, S.; Chen, X.; Zhou, J.; Shao, X.; Wang, C.: 3D transient multiphase model for keyhole, vapor plume, and weld pool dynamics in laser welding including the ambient pressure effect. *Opt. Lasers Eng.* **74**, 47–58, 2015
68. Qiu, C.; Panwisawas, C.; Ward, M.; Basoalto, H.C.; Brooks, J.W.; Attallah, M.M.: On the role of melt flow into the surface structure and porosity development during selective laser melting. *Acta Mater.* **96**, 72–79, 2015
69. Liu, Y.J.: Microstructure, defects and mechanical behavior of beta-type titanium porous structures manufactured by electron beam melting and selective laser melting. *J. Mech. Behav. Biomed. Mater.* **60**(4), 65–83, 2016